

# Investigation of slag-refractory interactions for the Ruhrstahl Heraeus (RH) vacuum degassing process in steelmaking

Mun-Kyu Cho<sup>a</sup>, Marie-Aline Van Ende<sup>b</sup>, Tae-Hee Eun<sup>a</sup>, In-Ho Jung<sup>b,\*</sup>

<sup>a</sup> Research Institute of Industrial Science and Technology, San 32, Hyoja-dong, Nam-gu Pohang, Gyeongbuk 790-600, Republic of Korea

<sup>b</sup> Dept. Mining and Materials Engineering, McGill University, 3610 University Street, Montreal QC H3A 2B2, Canada

Received 20 October 2011; received in revised form 14 December 2011; accepted 7 January 2012

Available online 10 February 2012

## Abstract

In order to determine the effect of slag composition during the RH process on refractory wear, magnesia–carbon and magnesia–chromite refractories were immersed for 10 min at 1600 °C in a ladle slag, two FeO-rich slags (20 and 40 wt% FeO) and two CaO–Al<sub>2</sub>O<sub>3</sub> slags. Corrosion of magnesia–carbon refractory by the ladle and CaO–Al<sub>2</sub>O<sub>3</sub> slags was limited as the refractory carbon phase efficiently prevented slag infiltration. Severe degradation was observed in contact with FeO-rich slags. FeO oxidized the carbon phase with formation of Fe droplets at the hot face. Regarding magnesia–chromite refractory, the corrosion mechanism consisted of severe slag infiltration, high temperature inactivation of the secondary chromite and primary chromite dissolution in the infiltrating slag. The FeO-rich slags seem to have generated more severe conditions as the infiltrating slag pushed apart the periclase grains, leading to severe refractory erosion. The degradation mechanisms are discussed by combining experimental results and thermodynamic calculations.

© 2012 Elsevier Ltd. All rights reserved.

**Keywords:** Corrosion; Refractories; Magnesia–carbon; Magnesia–chromite; FeO-rich; CaO–Al<sub>2</sub>O<sub>3</sub> slags

## 1. Introduction

The Ruhrstahl Heraeus (RH) degassing vessel is an important metallurgical reactor involving complex reactions between molten steel, gas, slag, inclusions and refractory. The refractory lining in the RH vessel and in the snorkels are subjected to severe corrosion conditions due to the high liquid steel circulation between the RH vessel and the ladle, the chemical reactions in the RH vessel, the violent temperature change, the O<sub>2</sub> blowing and vacuum conditions, etc. The choice of adequate materials for the RH lining is therefore of high importance to extend the RH lining life. In particular, the RH process for high Mn and high Si steels causes more severe corrosion conditions for the RH refractory lining.

Recently the present authors<sup>1</sup> proposed a new approach to model the complex industrial RH process using thermodynamic database and simplified kinetic expressions to account for the process dynamics. The model is based on effective equilibrium

reaction zone volumes. In this approach, all phases within the ‘effective’ reaction zone located at a reaction interface are assumed to reach equilibrium. This approach allows easy linkage of the thermodynamic database to the kinetic simulation. Depending on the process conditions, the extent of the effective reaction zone volume changes to consider the variations in reaction kinetics. The RH degassing process was divided into 14 effective reaction zones. The evolution of the effective reaction zone volumes as a function of the RH process conditions was determined based on physical descriptions of the different reaction mechanisms. Simplified mathematical functions and empirical relations derived from previous CFD/numerical simulation studies and plant data were used to constrain the effective reaction zone volume. Thermodynamic equilibrium at each reaction zones and each cycle was calculated using FactSage software<sup>2</sup> (version 6.1). Only a few model parameters were introduced to reproduce the evolution of the O and C contents in the steel based on industrial sampling data. The model is able to successfully reproduce the industrial data for various steel compositions and process conditions.

The results of the model were used to clarify the decarburization behavior observed during the treatment. Industrial data

\* Corresponding author. Tel.: +1 514 398 2608; fax: +1 514 398 4492.  
E-mail address: [in-ho.jung@mcgill.ca](mailto:in-ho.jung@mcgill.ca) (I.-H. Jung).

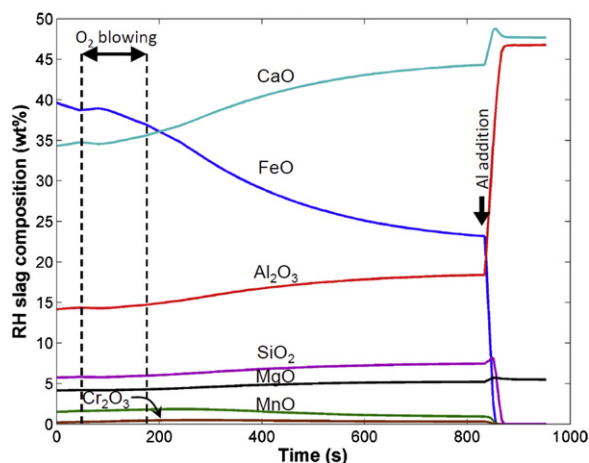


Fig. 1. Evolution of the calculated RH slag composition during the RH degassing treatment of low-carbon steel.

show a considerable deviation from the stoichiometric decarburization reaction trajectories, in particular towards an increase of the O content. An RH slag can be formed in the RH vessel due to the entrainment of ladle slag during the immersion of the RH snorkels into the ladle and the dissolution of  $\text{Fe}_t\text{O}$  attached on the RH vessel wall after the previous batch of the RH process. The RH slag contains a large amount of  $\text{Fe}_t\text{O}$  originating from oxidation of the steel skull and metal droplets in the RH vessel and steel oxidation during the  $\text{O}_2$  blowing stage. Fig. 1 shows the predicted RH slag composition during the process. As the decarburization reaction proceeds, the amount of RH slag and the  $\text{Fe}_t\text{O}$  concentration decrease continuously to supply O towards steel. After decarburization reaction, Al is added to deoxidize the molten steel containing high oxygen, and subsequently,  $\text{Fe}_t\text{O}$  content in slag decreases and  $\text{Al}_2\text{O}_3$  content increase.

According to the model predictions, the RH slag contains a high  $\text{Fe}_t\text{O}$  level during the first 15 min of the RH process (between 40 and 22 wt% FeO).  $\text{Fe}_t\text{O}$  is known to be aggressive towards most of the typical refractory lining materials. The impact of such high  $\text{Fe}_t\text{O}$  content in the RH slag on the refractory lining needs to be carefully examined. During the Al addition, the reducible components in the slag including  $\text{Fe}_t\text{O}$ ,  $\text{SiO}_2$ ,  $\text{MnO}$  and  $\text{Cr}_2\text{O}_3$  are reduced by Al. After the Al addition, the RH slag becomes a  $\text{CaO-Al}_2\text{O}_3$  slag containing some  $\text{MgO}$ .

In the present study, the corrosion behavior of two common refractories, i.e. magnesia–chromite and magnesia–carbon, in contact with various RH slags were experimentally investigated. Five slag compositions were selected to simulate the major slag composition changes in the RH vessel during the degassing process: a typical ladle slag, two FeO-rich slags and two  $\text{CaO-Al}_2\text{O}_3$  slags.

## 2. Experimental

### 2.1. Experimental setup and procedure

The slag samples were obtained from mixture of reagent grade oxide powders. Their compositions are listed in Table 1.

Table 1  
Composition of the synthetic slags (wt%).

Slag	Symbol	MgO	$\text{Al}_2\text{O}_3$	$\text{SiO}_2$	CaO	FeO
Ladle slag	L	5.3	27.7	10.7	56.3	0.0
FeO-rich slag 1	F1	4.2	22.2	8.6	45.0	20.0
FeO-rich slag 2	F2	3.2	16.6	6.4	33.8	40.0
$\text{CaO-Al}_2\text{O}_3$ slag 1	C1	0.0	45.0	0.0	55.0	0.0
$\text{CaO-Al}_2\text{O}_3$ slag 2	C2	0.0	60.0	0.0	40.0	0.0

Slag L is a typical ladle slag composition. The FeO-rich slags F1 and F2 were chosen to simulate the chemical reactions between RH refractory and high FeO slag in the RH vessel after the oxygen blowing stage and before Al deoxidation. The compositions of F1 and F2 were obtained by adding, respectively, 20 and 40 wt% FeO to slag L. The  $\text{CaO-Al}_2\text{O}_3$  slags C1 and C2 are representative of the RH slag composition after Al deoxidation until the end of the RH process. Slag C1 is a CaO-saturated liquid calcium aluminate slag, whereas slag C2 is saturated with respect to  $\text{Al}_2\text{O}_3$ .

The refractory samples were cut from commercially available refractory bricks in cylinders of about 13 mm diameter and 50 mm length. The  $\text{MgO-C}$  refractory was heat treated at  $1400^\circ\text{C}$  for 1 h in a graphite crucible in order to decompose the binders and transform the metal and  $\text{MgO}$  powders into spinel. The overall composition and apparent porosity of the investigated refractories are given in Table 2.

The experiments were carried out using an induction furnace under purified Ar gas (gas purification system and Mg turning furnace). About 400 g of premixed slags were filled in a crucible in the induction furnace.  $\text{MgO}$  crucibles were used for the FeO-rich slags F1 and F2 and graphite crucibles were used for all the other slags. The refractory sample was fixed on a Mo rod and placed near the top of the furnace. Once the slag melted at  $1600^\circ\text{C}$ , the refractory sample was moved down and maintained above the crucible for 30 min to preheat the brick. The refractory sample was subsequently immersed in the molten slag for 10 min. As a typical RH degassing process is about 20–25 min with Al addition performed at 10–15 min (Fig. 1), the contact time between slag and refractory in the experiments was fixed at 10 min to represent the actual interaction time between slag and the RH vessel lining during the RH process. After 10 min, the refractory sample was removed from the melt and quenched. The slag was cooled down to room temperature by switching off the power. This procedure was repeated for each combination of slag and refractory listed in Tables 1 and 2.

After the corrosion experiment, the refractory samples were mounted in resin, cut along the vertical direction, polished and coated with a conductive carbon layer. Microstructural observations and chemical analyses were obtained with a high-resolution scanning electron microscope (Philips SEM XL-30 FEG), equipped with an Energy Dispersive Spectroscopy (EDS) detector system from EDAX. Final slags after the tests were analyzed with a wavelength-dispersive X-ray fluorescence spectrometer (WDXRF) from Rigaku.

Table 2

Overall composition and apparent porosity of the investigated refractories.

Refractory	Overall composition (wt%)							Apparent porosity (%)
	MgO	Cr <sub>2</sub> O <sub>3</sub>	CaO	SiO <sub>2</sub>	Al <sub>2</sub> O <sub>3</sub>	FeO <sub>t</sub>	C	
Magnesia–chromite	55.8	22.9		2.1	8.2	11.0		16–17
Magnesia–carbon	90.3		0.8	2.2	6.8		5.1	11–13

## 2.2. Thermodynamic calculations

Thermodynamic calculations were performed with the FactSage software version 6.2.<sup>2</sup> Equilibrium calculations were performed with the equilibrium module EQUILIB, which is based on the minimization of the Gibbs free energy, and the FACT database. The solutions considered in the calculations are FToxid-SLAGA (slag), FToxid-SPINA (spinel solution of MgAl<sub>2</sub>O<sub>4</sub>–MgCr<sub>2</sub>O<sub>4</sub>–FeAl<sub>2</sub>O<sub>4</sub>–Fe<sub>3</sub>O<sub>4</sub>, etc.), FToxid-MeO (monoxide solution of CaO–MgO–FeO, etc.), FTmisc-FeLq (molten steel) and FACT53 (gas phase). Argon (0.1 g) was included in the calculations to consider the atmosphere surrounding the samples. The slag–refractory interactions were modeled at 1600 °C by relative addition of refractory ( $x$ , in g) to the slag ( $(1-x)$ , in g). Therefore, the X axis of the prediction diagrams roughly represents the interdiffusion of slag and refractory at the interface: the left side being the bulk slag ( $x=0$ ) and the right side the original refractory ( $x=1$ ). The slag and refractory compositions were taken from Tables 1 and 2, respectively. The composition of the magnesia–carbon refractory was simplified to a MgO–C mixture containing 5.13 wt% C.

## 3. Results and discussion

### 3.1. Degradation of magnesia–carbon refractories

The as-delivered microstructure of the magnesia–carbon refractory is shown in Fig. 2 and consists of large fused periclase grains, small sintered periclase grains bonded by graphite flakes, Si–Al metal particles (from antioxidants) and calcium silicate phase as intragranular impurities in the large periclase

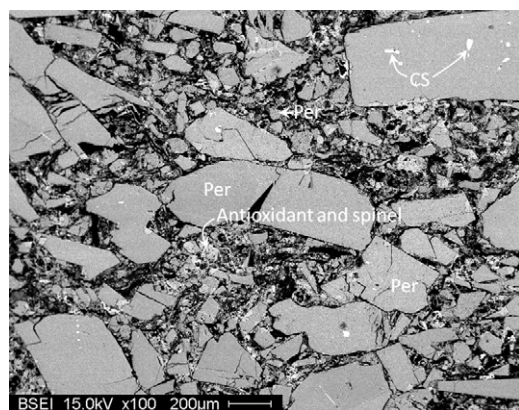


Fig. 2. BSE images of the as-delivered magnesia–carbon microstructure (Per=periclase grains; CS=calcium silicate impurity). The graphite phase is shown in black.

grains. MgO–Al<sub>2</sub>O<sub>3</sub> spinel phases formed by oxidation of the antioxidants are observed frequently near the Si-rich metal particles.

Fig. 3 shows back-scattered electron (BSE) images of the magnesia–carbon sample cross-sections after immersion in ladle slag L, FeO-rich slags F1 and F2 and CaO–Al<sub>2</sub>O<sub>3</sub> slag C2. The extent of slag attack on the refractory samples can be clearly seen. The overall compositions of the slags after the immersion tests with magnesia–carbon refractories are listed in Table 3.

#### 3.1.1. Ladle slag (L), and CaO–Al<sub>2</sub>O<sub>3</sub> slags C1 and C2

In the case of the ladle slag L and the CaO–Al<sub>2</sub>O<sub>3</sub> slags C1 and C2, the overall corrosion rate of the magnesia–carbon refractory samples is very limited. The sample cross-sections in Fig. 3 were taken near the sample tip. Macroscopic observations of the samples revealed that the shape of the refractory samples is preserved after the immersion tests. Penetration of these slags in the brick is effectively halted by the refractory carbon phase due to its non-wetting character. Detailed views of the refractory hot face of the samples in contact with slags L, C1 and C2 are shown in Fig. 4. The extent of the refractory hot face is less than 500 µm. No metal particles or evidences of reactions between these slags and the refractory phases were observed. As seen in Table 3, the composition of the slags L, C1 and C2 is very close to the initial compositions given in Table 1. The local MgO content at the refractory hot face of the samples immersed in slags C1 and C2 is in average about 4–5 wt%, with maximum up to 10 wt%.

Fig. 5 shows the predicted chemical stability and the equilibrium composition of the slags L, C1 and C2 in contact with magnesia–carbon refractory. The thermodynamic calculations predict the formation of a (Mg,Ca)O solid solution with CaO content less than 1 wt% in equilibrium with the three slags L, C1 and C2, causing a steady decrease of CaO from the slag (Fig. 5) as the relative amount of refractory increases. In the case of slag L (Fig. 5(a) and (b)), no severe reactions occur as the slag is already MgO saturated (calculated MgO saturation is 5.4 wt%). The periclase phase is stable with the initial slag at  $x=0$ , which

Table 3

XRF analyses of the slag samples after the immersion tests with magnesia–carbon refractory (in wt%).

Slag	MgO	Al <sub>2</sub> O <sub>3</sub>	SiO <sub>2</sub>	CaO	Cr <sub>2</sub> O <sub>3</sub>	“FeO”
L	5.7	27.6	9.7	54.1	0.0	0.1
C1	0.5	40.8	0.4	57.7	0.0	0.1
C2	0.3	67.5	0.3	31.5	0.0	0.1
F1	4.8	19.7	13.5	41.3	0.1	17.5
F2	3.7	16.2	9.6	32.0	0.1	33.5



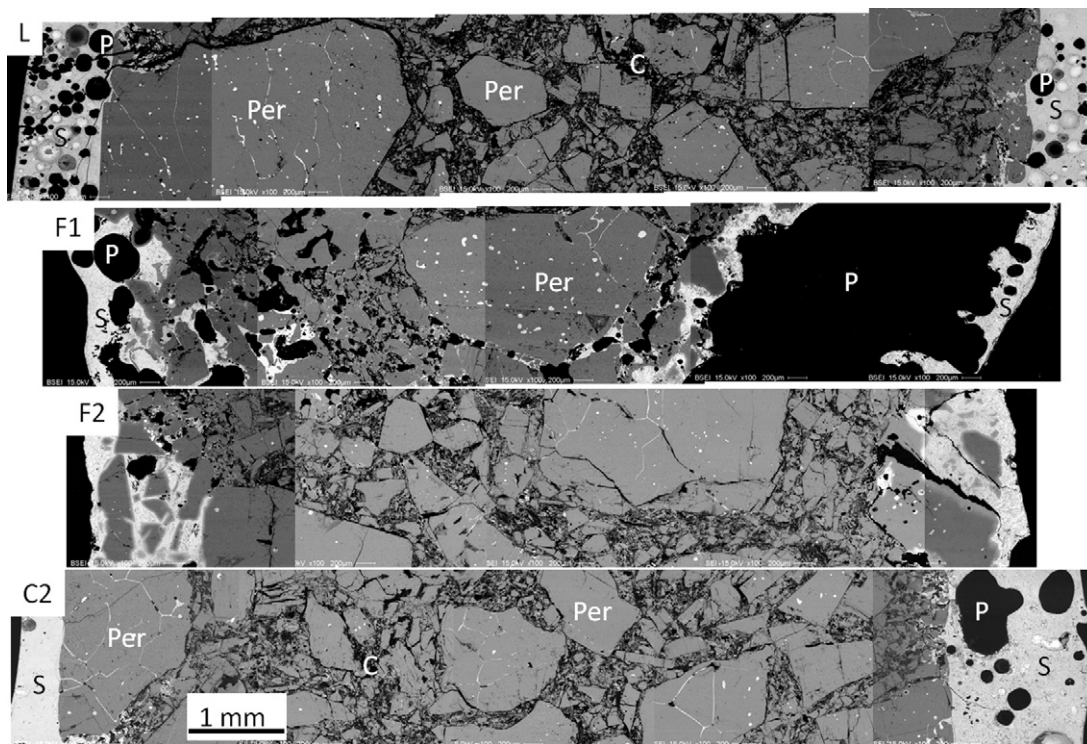


Fig. 3. BSE images of the magnesia–carbon sample cross-section after immersion in the slags L, F1, F2 and C2 (Per = periclase grains; P = pore; C = graphite phase; S = slag).

is corroborated by the experimental observations. In the case of slags C1 (Fig. 5(c) and (d)) and C2 (Fig. 5(e) and (f)), the predictions show that the periclase phase is unstable with the initial slags ( $x = 0$ ). The refractory periclase phase is dissolved until the MgO content in the slags reaches MgO saturation. The calculated MgO saturation for slags C1 and C2 is, respectively, 7.1 and 13.7 wt% MgO. The degradation of the magnesia–carbon refractory should therefore be the highest with slag C2 as the difference between the initial MgO content and that at equilibrium, i.e. the driving force for MgO dissolution, is the largest. The refractory carbon phase does not react with any of the three investigated slags (Fig. 5(a), (c) and (e)). Only a small amount of carbon is consumed through the MgO–C reaction, producing Mg(g) and CO(g).

The main degradation mechanism for slags C1 and C2 is therefore the dissolution of MgO from the refractory to the unsaturated slag. From the experimental observations, only a limited increase of the MgO content at the refractory hot face was found. No significant MgO increase was measured in the bulk slag after the experiments (Table 3) and the overall sample degradation is very limited. Kinetic factors would therefore have played an important role.

### 3.1.2. FeO-rich slags F1 and F2

In the case of the FeO-rich slags F1 and F2, the overall corrosion rate of the magnesia–carbon refractory is much more severe, as seen in Fig. 3. The refractory samples were considerably damaged during the tests and parts of the refractory sample detached during the experiments upon the actions of slag attack and turbulences in the melt created by the induction. The

cross-sections shown in Fig. 3 could not be taken near the sample tip to compare with the other samples. As seen in Fig. 3, the slags F1 and F2 significantly penetrated into the refractory sample. Detailed views of the refractory hot face are provided in Fig. 6.

At the hot face of the refractory sample in contact with slag F1 (Fig. 6(a) and (b)), small iron metal particles ( $<10 \mu\text{m}$ ) are present. The periclase grains at the refractory hot face in contact with the FeO-rich slags undergoes an increase of the FeO content (up to 15 wt% FeO), changing the MgO grains into a (Mg,Fe)O solid solution. The Fe uptake in the periclase grains at the refractory hot face is clearly seen in the BSE micrographs in Fig. 6(a) and (b). The small MgO grains and the edges of large ones are brighter than the unreacted periclase as Fe with higher atomic number diffuses in the MgO grain. The slag attached on the refractory samples contains between 17 and 20 wt% FeO and is inhomogeneous (left side of Fig. 6(a)). The FeO-rich slag has infiltrated the decarburized areas, causing the erosion of the periclase grains into the slag. The slag becomes depleted in FeO (10–15 wt%) as one moves to the inner side of the hot face (Fig. 6(b)).

As seen in Fig. 6(c) and (d), larger and more numerous iron metal particles were found at the refractory hot face after immersion in the FeO-rich slag F2. Similar to the sample in contact with slag F1, the small MgO grains and the edges of the larger ones at the refractory hot face are brighter than the unreacted ones as they undergo a significant Fe uptake. At the edge of the large periclase grains, the FeO content reaches 30 wt%. As shown in Fig. 6(d), the FeO-rich slag has infiltrated the decarburized area, filling the space between the MgO grains. The slag in-between

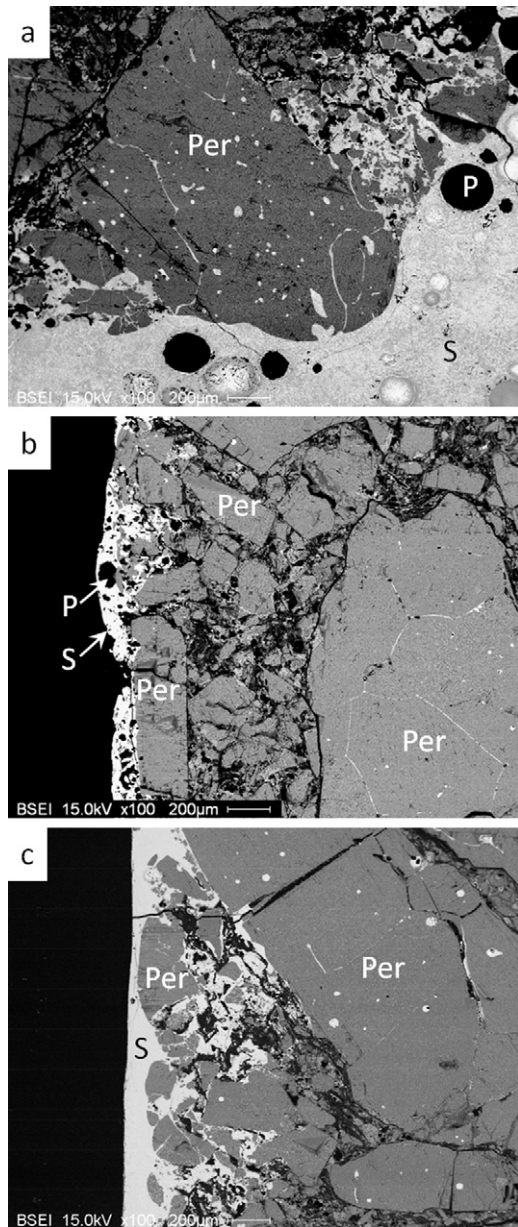


Fig. 4. Enlarged view (BSE images) of the magnesia–carbon refractory hot face after immersion in slags (a) L, (b) C1 and (c) C2 (Per = periclase grains; P = pore; S = slag).

the (Mg,Fe)O grains in Fig. 6(d) is significantly depleted in FeO (5–10 wt%) while the (Mg,Fe)O grains contains between 20 and 30 wt% FeO. As seen in Fig. 6(c), the MgO grains are washed away from the refractory as the slag infiltrates in the decarburized areas. As a consequence of Fe uptake in the periclase grains and Fe metal droplet formation, the FeO content in the bulk slags F1 and F2 after the immersion tests is decreased by several % compared to the original content (Tables 1 and 3).

Fig. 7 shows the calculated refractory stability, and equilibrium compositions of the slag and periclase solid solution (magnesio-wustite) for slags F1 and F2 in contact with magnesia–carbon refractory. As seen in Fig. 7(a) and (d), both slags are unstable with the refractory periclase phase. The periclase dissolves into the slag until the slag reaches MgO saturation

(Fig. 7(b) and (e)). The calculated MgO saturation is 6.7 and 7.1 wt% for, respectively, slags F1 and F2. An iron-rich liquid metal phase forms in the refractory, and its amount increases with the FeO content in slag (Fig. 7(a) and (d)). This liquid metal phase is composed mainly of Fe with some dissolved O and C at high slag dilution. The refractory carbon phase can be completely consumed at more than 50% of the refractory. The carbon phase becomes stable only when the slag amount decreases. Its stability decreases with increasing the FeO content in the slag from F1 to F2. When the carbon phase is stable, the liquid metal is carbon saturated with some dissolved Al and Si. The predicted FeO content in slag, as shown in Fig. 7(b) and (e), decreases quickly with increasing the fraction of refractory. This decrease is due to the formation of an iron metal phase and a (Mg,Fe)O solid solution as observed in the sample microstructures. The equilibrium composition of the solid solution is depicted in Fig. 7(c) and (f) for, respectively, slags F1 and F2. A high FeO content in the slag will bring a high FeO content in the solid solution. The maximum FeO content in the solid solution in contact with slags F1 and F2 is calculated to be 13.9 and 29.5 wt%, respectively. These equilibrium values are in good agreement with those measured in the (Mg,Fe)O grains. The FeO content in the magnesio-wustite solid solution decreases sharply with increasing the amount of refractory owing to the presence of the refractory carbon phase that reduces FeO.

Compared to the thermodynamic calculations with slags L, C1 and C2, the reactions between the refractory and FeO-rich slags (F1 and F2) are more severe as both refractory phases MgO and carbon are attacked by FeO in the slags. The predicted reactions are in good agreement with the observations.

### 3.1.3. Corrosion mechanisms

The corrosion mechanisms of magnesia–carbon refractories by various slags have been investigated by many researchers.<sup>3–15</sup> Magnesia–carbon refractories are among the most successful materials for primary steelmaking applications owing to its high thermal shock resistance and high slag corrosion resistance. The latter is mainly due to carbon's non-wettability towards slag, which limits liquid slag penetration. However, magnesia–carbon refractories are highly vulnerable to oxidation. The main mechanisms leading to the oxidation of the refractory carbon phase include:

- Direct and indirect carbon oxidation,<sup>3–8</sup> in which, respectively, the refractory carbon reacts with O<sub>2</sub> present in the gas phase and with the refractory MgO, according to the following reactions:
 
$$\text{C(s)} + \frac{1}{2}\text{O}_2\text{(g)} = \text{CO(g)} \quad (1)$$

$$\text{MgO(s)} + \text{C(s)} = \text{Mg(g)} + \text{CO(g)} \quad (2)$$
- Reaction between refractory carbon and reducible slag components MO, such as FeO<sub>x</sub>, CrO<sub>x</sub>, MnO, SiO<sub>2</sub>, etc. according to the reaction<sup>13,14</sup>:
 
$$\text{C(s)} + \text{MO}_{\text{slag}} = \text{M(l)} + \text{CO(g)} \quad (3)$$



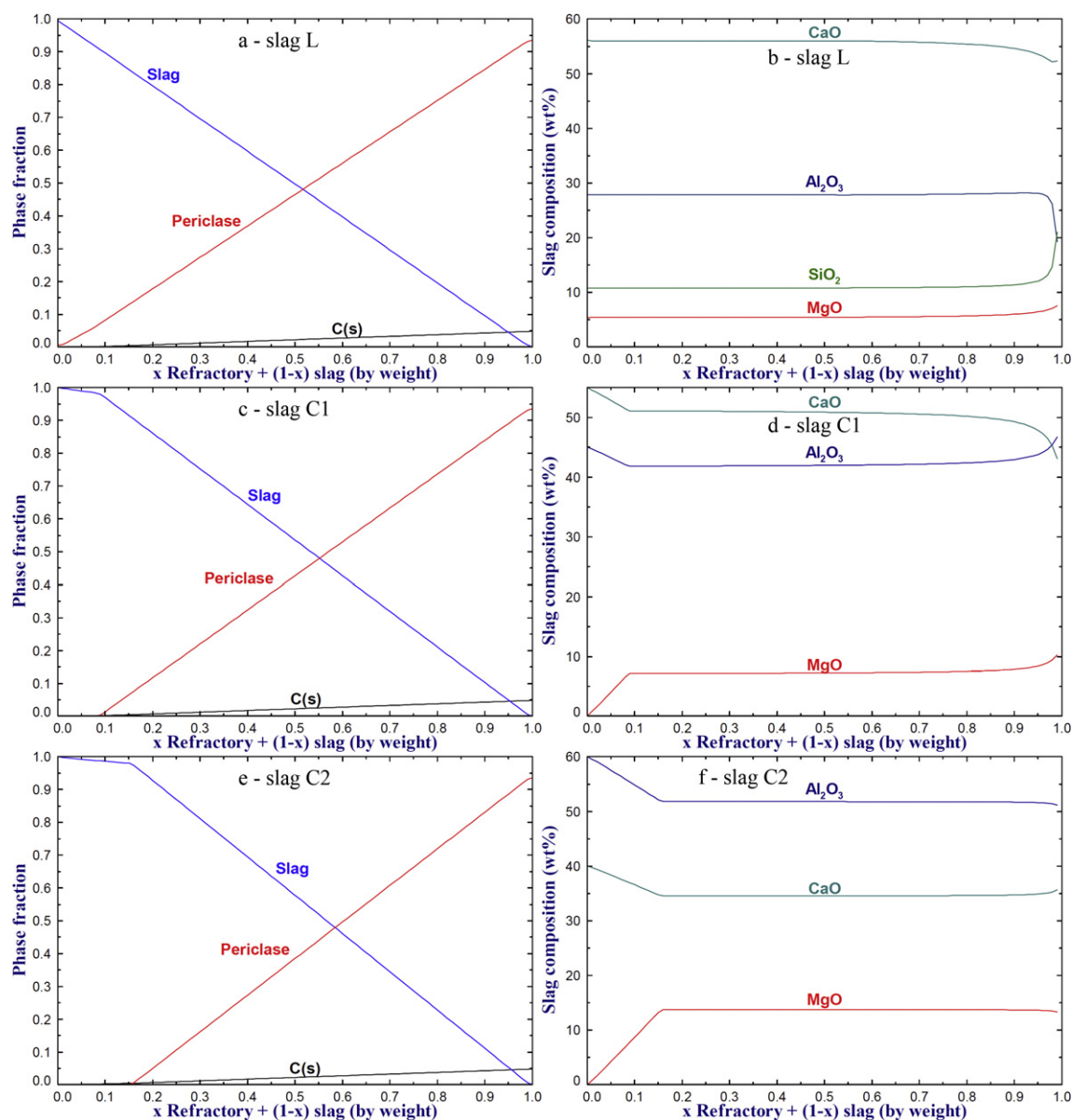


Fig. 5. Predicted chemical stability of magnesia-carbon refractory and slag composition in contact with (a) and (b) slag L; (c) and (d) slag C1, (e) and (f) slag C2.

Once a decarburized layer is formed, the slag is able to infiltrate the refractory, and subsequently dissolve and erode the refractory periclase grains. Another critical parameter which greatly influences the degradation of MgO-based refractories is the MgO content in molten slag. Attaining the MgO saturation in the slag is essential to avoid the fast dissolution of MgO grains in the liquid slag.

Under the present experimental conditions, the direct and indirect carbon oxidation mechanisms were less significant. The low  $O_2$  content in the gas phase combined with the slow removal of the gaseous reaction products and the  $CO(g)$  build-up at the refractory interface may slow down or even prevent reactions (1) and (2) to occur. On the other hand, numerous Fe metal particles were found within the hot face of the worn samples in contact with slags F1 and F2, while no such metal particles were observed in the samples in contact with slags L, C1 and C2. With increasing the FeO content from 20 to 40 wt% (F1 to

F2), the amount and size of Fe metal particles have increased. The high FeO content in slags F1 and F2 caused the occurrence of reaction (3). As a result, a large decarburized layer is formed at the slag refractory interface, which has been infiltrated by the slag (Fig. 6). As observed in the worn microstructures, the MgO grains in the decarburized layer are then exposed to the slag, leading to their dissolution and erosion to the slag. FeO diffuses from the slag bulk to the infiltrating slag at the refractory hot face, leading to further oxidation of the carbon phase and subsequent slag penetration into the refractory.

The formation of the  $(Mg,Fe,Mn)O$  solid solution was reported to influence the slag penetration mechanism in MgO refractories by Zhang et al.<sup>16</sup> based on SEM investigations of worn samples in contact with EAF slag containing 17.5 wt%  $Fe_2O_3$  and BOF slags for 3 and 6 h. They observed an increase of the magnesio-wustite crystal size at the refractory interface, which caused lower slag penetration into the MgO refractory. In

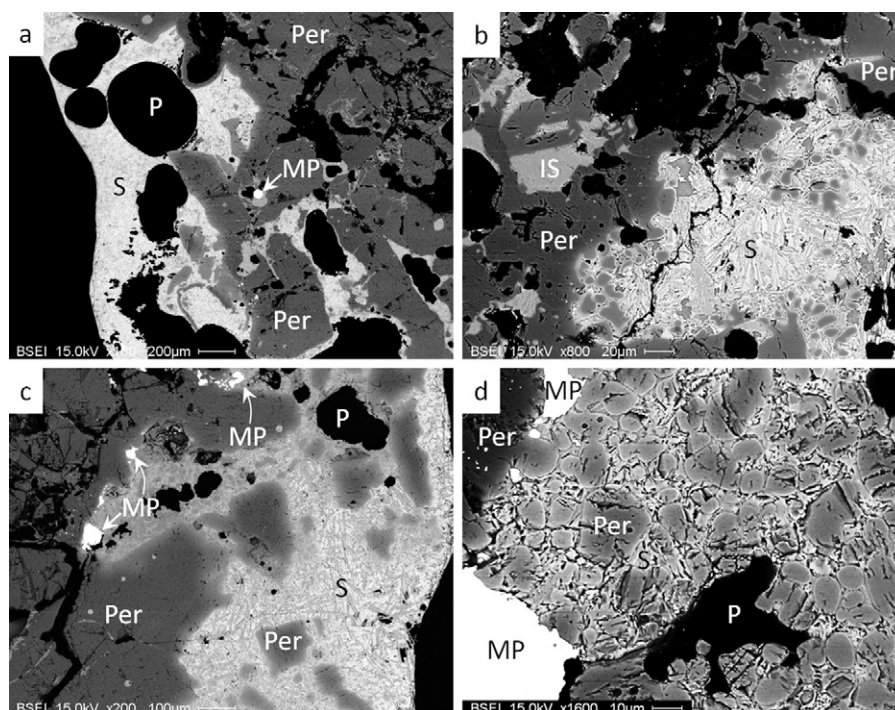


Fig. 6. Enlarged view (BSE images) of the magnesia–carbon refractory hot face after immersion in (a) and (b) slag F1 and (c) and (d) slag F2 (Per = periclase grains; P = pore; C = graphite phase; S = slag; MP = metal particle; IS = infiltrating slag).

the present study, no significant changes in size were observed among the (Mg,Fe)O crystals at the refractory interface. The immersion time (only 10 min) is presumed not long enough to observe the growth of the solid solution crystals.

### 3.2. Degradation of magnesia–chromite refractories

The as-delivered magnesia–chromite refractory consists of magnesia (periclase) and chromite spinel ((Mg,Fe)(Cr,Al)<sub>2</sub>O<sub>4</sub>) grains and CaO–MgO–SiO<sub>2</sub> phase at the grain boundaries. The chromites are classified into three types<sup>17–19</sup>: primary chromite, secondary chromite type I and secondary chromite type II. Primary chromite grains arise from the blended raw material and are present as large crystals in Fig. 8(a). Secondary chromite spinel grains are present as small crystals in Fig. 8(b). Type I is formed by intergranular precipitation upon cooling from magnesia grains or Cr-rich liquid and is located at grain boundaries, whereas type II arises via exsolution precipitation from magnesia grains upon cooling and is located within the magnesia grains. The nominal composition and apparent porosity of the refractory is given in Table 2. The chemical composition of each refractory phase, as determined by EDS analysis, is listed in Table 4. As seen in Fig. 8, the as-delivered material is characterized by a large network of interconnected pores. Based on the overall composition of the as-delivered material in Table 2, the refractory at equilibrium is calculated to be composed of 60.5% of periclase solution and 34.6% of spinel phase, the rest being a silicate phase. The predicted compositions of the phases are listed in Table 4. According to the thermodynamic calculations, FeO is principally dissolved in the periclase solid solution. In the as-delivered material, however, FeO is mainly in the chromite

Table 4

Chemical composition of the various refractory phases in the as-delivered magnesia–chromite refractory (in wt%).

Refractory phase	MgO	Al <sub>2</sub> O <sub>3</sub>	SiO <sub>2</sub>	CaO	Cr <sub>2</sub> O <sub>3</sub>	FeO
Periclase	94.2	0.4	0.7	0.2	2.1	2.5
Primary chromite	23.1	11.6	1.2	1.0	55.5	7.6
Secondary chromite type I	23.4	10.5	0.5	0.3	51.1	14.2
Secondary chromite type II	31.9	8.8	0.0	0.0	46.1	13.3
Silicate phase	32.0	0.1	38.4	27.8	0.8	0.9
Periclase (predicted)	75.2	<0.2	<0.2	<0.2	7.9	16.5
Spinel (predicted)	21.7	23.2	–	–	52.3	2.7

phase and the Al<sub>2</sub>O<sub>3</sub> content in the spinel is lower than the predicted values. At high temperature, the chromite phase in the refractory material will, therefore, tend to dissolve in the periclase solid solution.

An overview of the worn refractory cross-section in contact with slags L, C1, C2, F1 and F2 is shown in Fig. 9. The global compositions of the slags and average compositions of the infiltrating slag after the immersion tests with magnesia–chromite refractories are listed in Tables 5 and 6, respectively. Macroscopic wear of the refractory sample in contact with the slag

Table 5

XRF analyses of the slag samples after the immersion tests with magnesia–chromite refractory (in wt%).

Slag	MgO	Al <sub>2</sub> O <sub>3</sub>	SiO <sub>2</sub>	CaO	Cr <sub>2</sub> O <sub>3</sub>	“FeO”
L	6.0	28.5	10.8	53.2	0.2	0.2
C2	0.4	59.9	0.4	38.8	0.1	0.2
F1	4.9	19.4	12.9	41.5	0.8	17.6
F2	6.0	16.0	9.9	32.7	0.2	30.8

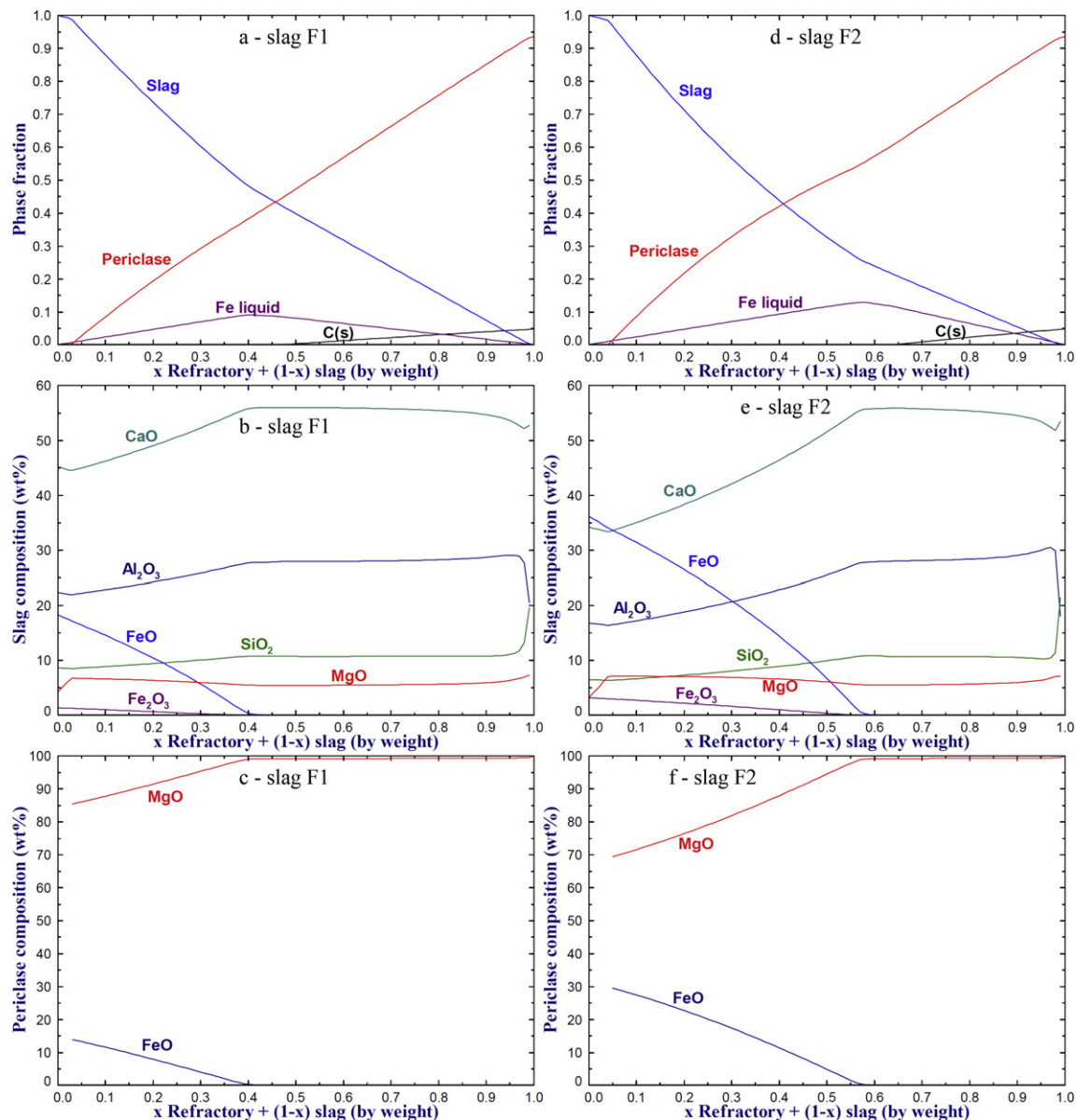


Fig. 7. Predicted chemical stability of magnesia–carbon refractory, slag composition and periclase composition in contact with (a–c) slag F1 and (d–f) slag F2.

L occurred mostly at the sample tip, which became rounded. As seen in Fig. 9, the worn refractory is completely infiltrated by the slag, filling most of the interconnected pores. Analysis of the slag revealed a FeO uptake in the infiltrating slag (~4 wt%), originating from the dissolution of chromite grains.

Table 6

Average composition of the infiltrating slag in magnesia–chromite refractory, as determined by EDS analysis (in wt%).

Slag	MgO	Al <sub>2</sub> O <sub>3</sub>	SiO <sub>2</sub>	CaO	Cr <sub>2</sub> O <sub>3</sub>	FeO
C1	2.8	28.4	7.8	44.8	2.4	13.8
C2a	5.1	48.4	0.7	39.3	1.0	5.6
C2b	4.6	34.6	8.0	41.6	2.1	9.2
F1	4.3	25.4	9.3	42.5	1.1	17.4
F2	5.9	16.5	7.6	41.3	2.4	26.3

### 3.2.1. CaO–Al<sub>2</sub>O<sub>3</sub> slags C1 and C2

Macroscopically, the wear of the two refractory samples immersed in slags C1 and C2 is limited. The overall shape of the refractory samples is preserved. Some bloating and cracking can be observed near the sample tip, especially in the sample in contact with slag C2. Microscopically, the refractory samples are entirely infiltrated by the slag through the interconnected pores, as seen in Fig. 9. The slag attached to the refractory is inhomogeneous and has a global composition close to the initial value, except for the increase in the MgO content (3–5 wt%). At the attached slag/refractory interface, the periclase and chromite grains were removed to the slag. A FeO, Cr<sub>2</sub>O<sub>3</sub>, MgO and SiO<sub>2</sub> pickup in the infiltrating slag was observed. However, the global slag composition after the tests is close to the initial one, without any significant increase in SiO<sub>2</sub>, FeO, Cr<sub>2</sub>O<sub>3</sub> or MgO.

Fig. 10(a) shows a detailed image of the slag infiltration at the center of the refractory sample by slag C1. The average



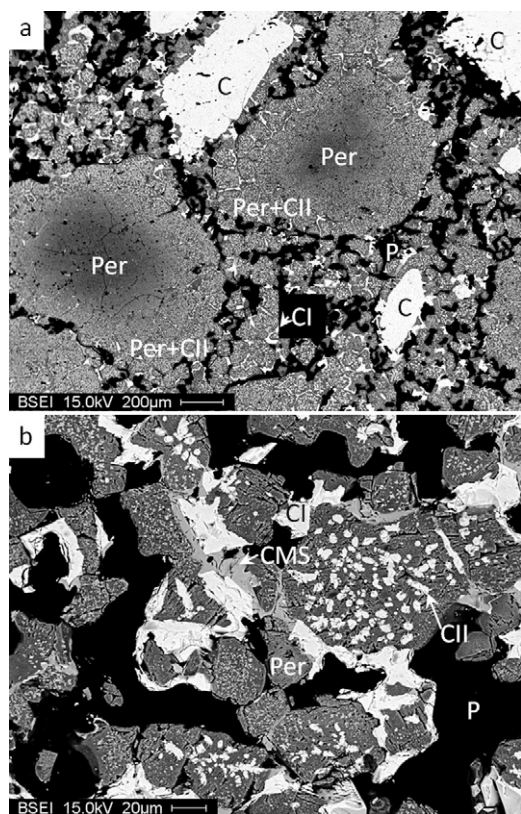


Fig. 8. (a and b) BSE images of the as-delivered magnesia–chromite refractory (Per=periclase; C=primary chromite; CI=secondary chromite type I; CII=secondary chromite type II; P=pore; CMS=CaO–MgO–SiO<sub>2</sub> phase).

composition of the infiltrating slag is listed in Table 6. Obviously, the increase of FeO and Cr<sub>2</sub>O<sub>3</sub> comes from the dissolution of the chromite phase into the infiltrating slag, while SiO<sub>2</sub> uptake originates from the dissolution of the CaO–MgO–SiO<sub>2</sub> phase originally present in the as-delivered refractory. The FeO content in the infiltrating slag increases rapidly from the slag/refractory interface and reaches a maximum approximately at the center of the refractory sample. The FeO content in the secondary chromite type I varies between 5 and 16 wt%. Also the FeO and Cr<sub>2</sub>O<sub>3</sub> contents in the periclase solid solution have increased to about 8 wt%. Slag infiltration in the center of the refractory sample in contact with slag C2 is depicted in Fig. 10(b). Similar to slag C1, the pores of the refractory are completely filled by the infiltrating slag. The latter exhibited two different compositions at the brick center, given in Table 6 as slags C2a and C2b. In infiltrating slag C2a shown in Fig. 10(b), the Al<sub>2</sub>O<sub>3</sub> content is higher than that of CaO, though much lower than the initial value (Table 1). A moderate FeO and Cr<sub>2</sub>O<sub>3</sub> pickup was measured. On the other hand, the infiltrating slag C2b became a CaO-rich slag with a larger increase in FeO, Cr<sub>2</sub>O<sub>3</sub> and SiO<sub>2</sub> originating from the dissolution of chromite grains and the original CaO–MgO–SiO<sub>2</sub> phase from the as-delivered material. The secondary chromite grains exhibit a significant increase in Al<sub>2</sub>O<sub>3</sub> content (up to 22 wt%) compared to that in the as-delivered material (Table 4). The difference between slags C2a and C2b is, therefore, due to the Al<sub>2</sub>O<sub>3</sub> uptake in the chromite phase. In average, the Al<sub>2</sub>O<sub>3</sub>, Cr<sub>2</sub>O<sub>3</sub> and

FeO contents in the periclase grains reach, respectively, 5.1, 9.0 and 4.5 wt%. As seen in Fig. 9, dissolution of the primary chromite grains occurred in both samples. Secondary chromite types I and II are still observed (Fig. 10), though the quantity was lower compared to that in the as-delivered material.

Figs. 11 and 12 present the thermodynamic predictions of the interactions between the magnesia–chromite refractory and slags C1 and C2, respectively. As seen in Figs. 11(a) and 12(a), slags C1 and C2 are unsaturated with respect to both refractory phases, i.e. the periclase solid solution and the spinel phase. For slag C1, the periclase solid solution is dissolved entirely until the slag reaches MgO saturation at 8.3 wt%. The spinel phase becomes stable soon after the periclase (Fig. 11(a)). As seen in Fig. 11(b), the Cr<sub>2</sub>O<sub>3</sub> content in the slag phase increases up to a maximum of 4.1 wt% which corresponds to the point where the spinel solution becomes stable, and then decreases continuously. Once the spinel phase is stable, the Cr<sub>2</sub>O<sub>3</sub> content in the periclase solid solution is mostly constant at about 8 wt% (Fig. 11(c)). FeO from both refractory phases (Fig. 11(c) and (d)) dissolves significantly in the slag, causing a continuous increase of the FeO content in slag with increasing the fraction of refractory (Fig. 11(b)) up to a maximum of 12.9 wt%. In the case of slag C2, the stability of the spinel phase in Fig. 12(a) exhibits a very different behavior. The spinel is rapidly stable (before the periclase solution) and present in large quantity compared to the four other slag systems. The reason for this is the presence of large amounts of Al<sub>2</sub>O<sub>3</sub> in the slag, which stabilizes the spinel phase by the formation of MgAl<sub>2</sub>O<sub>4</sub>–MgCr<sub>2</sub>O<sub>4</sub> solid solution. As seen in Fig. 12(b) and (d), the Al<sub>2</sub>O<sub>3</sub> content in the slag continuously decreases, whereas the Al content in the spinel increases. As a result, the original Al<sub>2</sub>O<sub>3</sub>-rich slag becomes a CaO-rich slag from  $x=0.64$ . As the spinel phase is rapidly stabilized in the refractory, the Cr<sub>2</sub>O<sub>3</sub> uptake in the slag is limited to a maximum of 1.5 wt%. The periclase solution is completely dissolved up to  $x=0.25$  when the slag reaches MgO saturation at 12.2 wt% MgO. The Cr<sub>2</sub>O<sub>3</sub> content in the periclase solid solution decreases to about 6 wt%. The FeO content in the slag increases continuously up to a maximum of 12.7 wt% (Fig. 12(b)), which originates from the periclase solid solution and the spinel phase (Fig. 12(c) and (d)). The SiO<sub>2</sub> and MgO contents in the slag increase sharply with increasing the fraction of refractory due to the dissolution of the refractory silicate phase in a very small amount of slag.

The thermodynamic predictions are, in general, in good agreement with the observations. A noticeable MgO, FeO and SiO<sub>2</sub> increase is measured in the infiltrating slags. The measured MgO content in the slag is, however, lower than the predicted saturation levels. Concerning the Cr<sub>2</sub>O<sub>3</sub> increase, the quantification is not very accurate due to the low concentrations (<1 wt% Cr). In general, the measured Cr<sub>2</sub>O<sub>3</sub> content in the periclase solid solution is higher than the predicted value, suggesting that Cr dissolves preferentially in the periclase than in the liquid slag. A significant amount of Al<sub>2</sub>O<sub>3</sub> dissolved in the periclase solid solution, which was not predicted. In case of slag C2, the change from an Al<sub>2</sub>O<sub>3</sub>-rich slag to a CaO-rich slag was observed (slags C2a and C2b). Also, an increase of Al<sub>2</sub>O<sub>3</sub> in the chromite grains was found. The formation of the additional spinel might

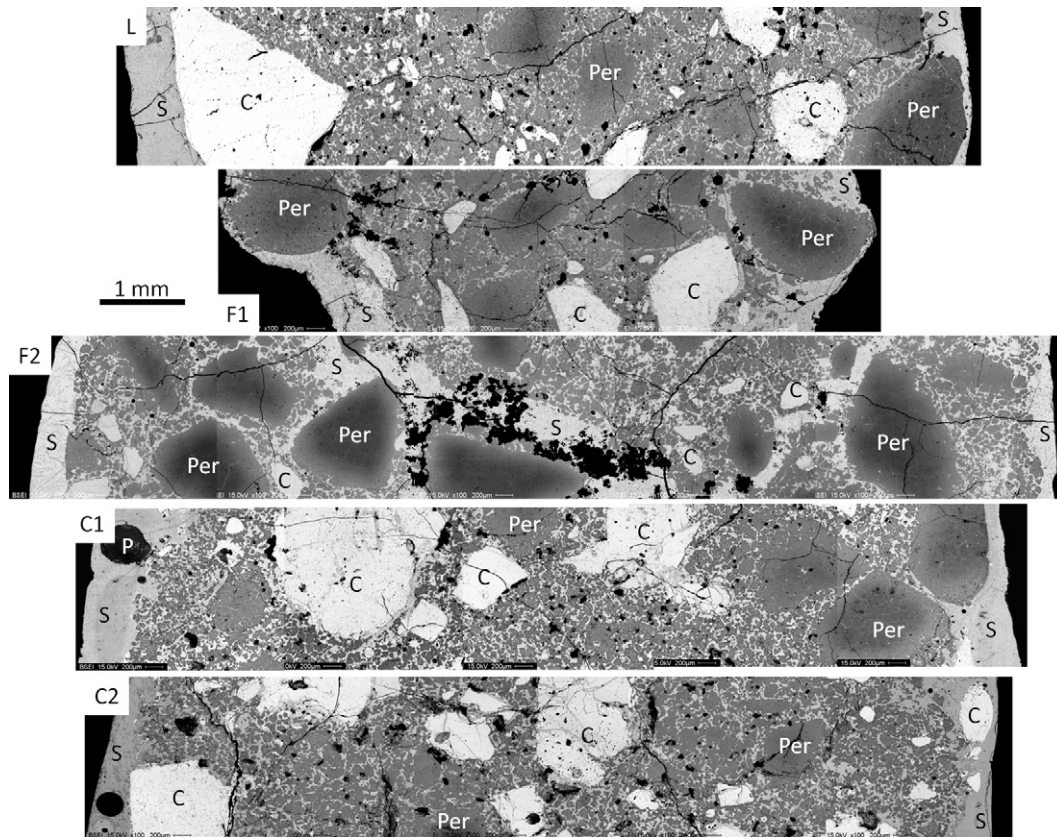


Fig. 9. BSE images of the magnesia–chromite sample cross-section after immersion in the slags L, F1, F2, C1 and C2 (Per = periclase grains; C = primary chromite; P = pore; S = slag).

be at the origin of the slight bloating and cracking observed macroscopically.

### 3.2.2. FeO-rich slags F1 and F2

The refractory samples in contact with slags F1 and F2 were mainly degraded at the tip. As seen in Fig. 9, the refractory was completely infiltrated by the slag. In the case of the sample immersed in slag F1, the tip was extremely damaged as the diameter of the sample is significantly diminished. However, it is unsure whether parts of the tip broke off during the experiment or during the sample preparation. In the case of the

sample in contact with slag F2, the tip appeared less damaged. However, the slag significantly infiltrated the refractory, creating large channels of infiltrating slag in the refractory microstructure. The grains forming the refractory appeared more pushed apart from each other than in the other samples. A similar mechanism might be at the origin of the break off of the refractory tip in contact with slag F1. This type of severe slag infiltration and separation of the grains by the infiltrating slag was observed only at the samples tip. At the middle of the refractory sample, the refractory is still entirely infiltrated by the slag, but the overall sample shape is preserved.

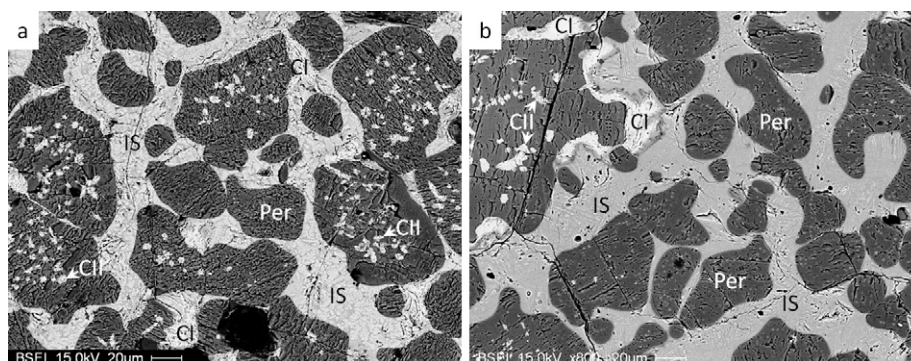


Fig. 10. Detailed view (BSE images) of the center of the magnesia–chromite refractory sample after immersion in the slags (a) C1 and (b) C2 (Per = periclase; CI = secondary chromite type I; CII = secondary chromite type II; IS = infiltrating slag).



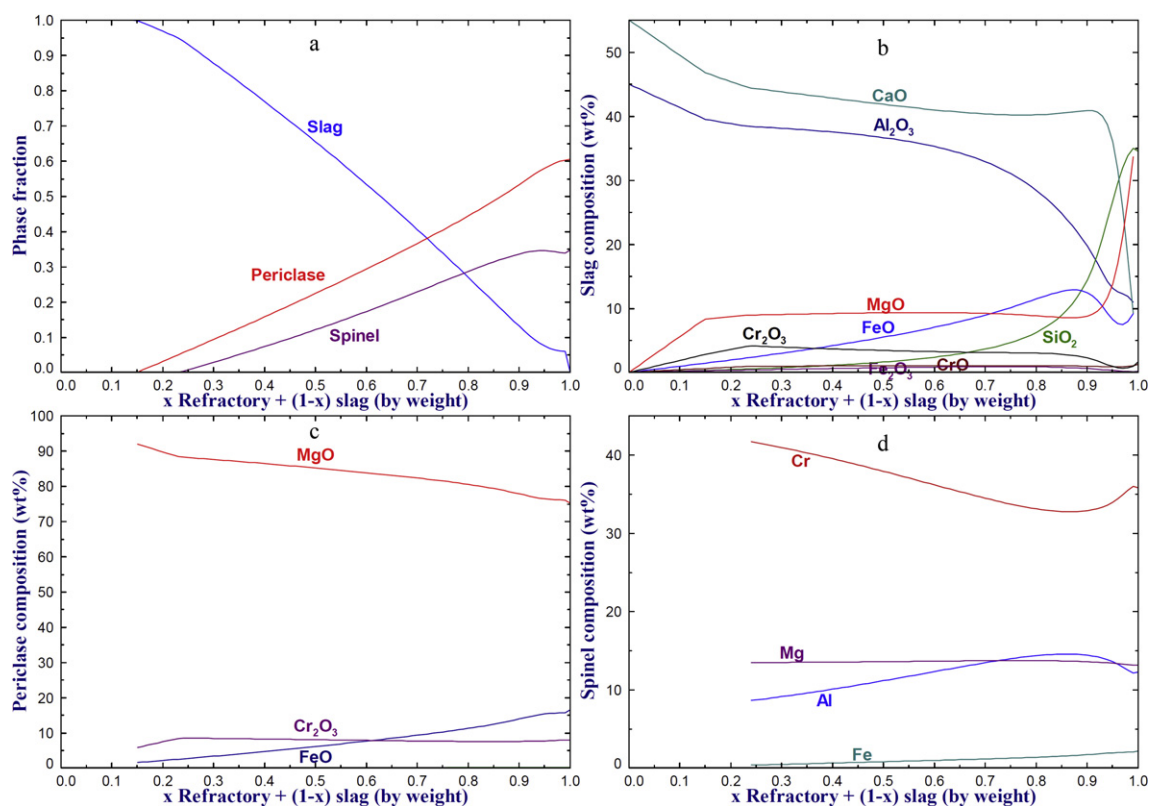


Fig. 11. (a) Predicted chemical stability and chemical composition of (b) slag, (c) periclase solid solution and (d) spinel after interaction between magnesia–chromite refractory and slag C1.

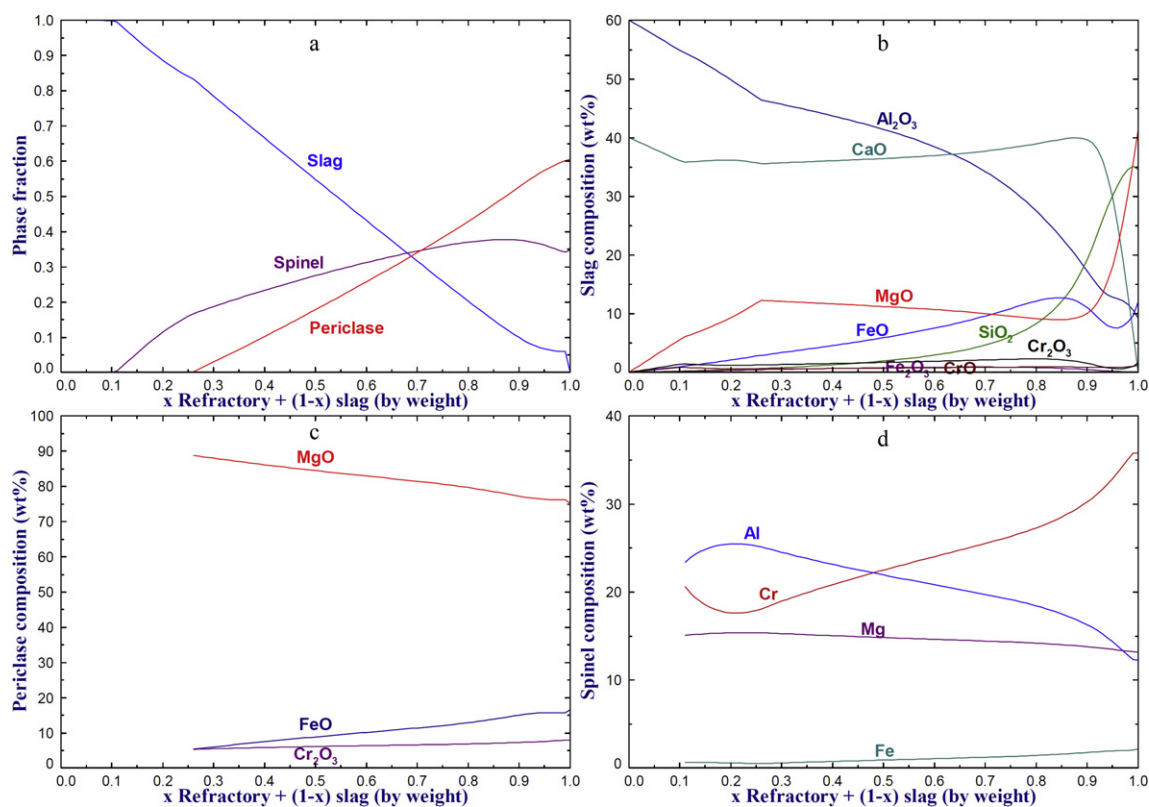


Fig. 12. (a) Predicted chemical stability and chemical composition of (b) slag, (c) periclase solid solution and (d) spinel after interaction between magnesia–chromite refractory and slag C2.



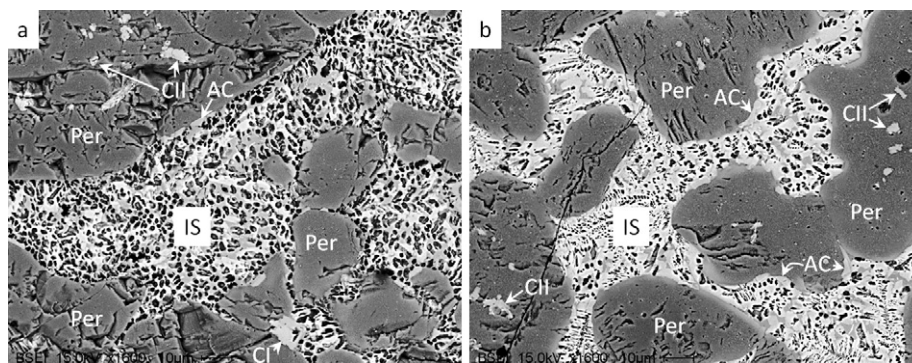


Fig. 13. Detailed view (BSE images) of the center of the magnesia–chromite refractory sample after immersion in the slags (a) F1 and (b) F2 (Per = periclase; CI = secondary chromite type I; CII = secondary chromite type II; IS = infiltrating slag; AC =  $\text{Al}_2\text{O}_3$ -rich chromite).

Detailed views of the center of the worn refractory in contact with slags F1 and F2 are given in Fig. 13(a) and (b), respectively. As seen in Fig. 13, the slag has infiltrated the interconnected pores between the periclase grains. The infiltrating slag is inhomogeneous and its overall composition is listed in Table 6. In the case of slag F1, the FeO content in the infiltrating slag has slightly decreased compared to the initial 20 wt%. The FeO and  $\text{Cr}_2\text{O}_3$  contents in the periclase solid solution have risen to, respectively, 9.6 wt% and 15.2 wt%. Similar contents in the solid solution are measured in the sample in contact with slag F2 (10.1 wt% FeO and 16.3 wt%  $\text{Cr}_2\text{O}_3$ ). A small Cr pickup in the infiltrating slag was measured for both slags F1 and F2, which mostly comes from the dissolution of the refractory secondary chromite phase. No significant increase in the  $\text{SiO}_2$  and  $\text{Al}_2\text{O}_3$  contents has occurred in the infiltrating slag. In the case of slag F2, the FeO content in the infiltrating slag has significantly decreased compared to its initial value (Tables 1 and 6). Small  $\text{Al}_2\text{O}_3$ -rich chromite phase ( $\sim 22.9$  wt%  $\text{MgO}$ –22.5 wt%  $\text{Al}_2\text{O}_3$ –35.5 wt%  $\text{Cr}_2\text{O}_3$ –16.6 wt% FeO) forms at the interface between the infiltrating slag and the solid solution grains (Fig. 13(a) and (b)). As seen in Fig. 13(b), the edges of the periclase grains are brighter due to the Fe uptake in the solid solution. The FeO content at the periclase grain edges reaches 25 wt%. For both slags, the primary chromite grains are moderately attacked by the infiltrating slag, whereas the amount of secondary chromite was considerably lower, especially at the sample tip. Compared to the worn samples in contact with slags C1, C2 and L, these samples in contact with FeO-rich slags seem more severely degraded. The infiltrating slag seems to have pushed apart the refractory grains, leading to a severe erosion of the refractory grains into the bulk slag.

Figs. 14 and 15 present the thermodynamic predictions of the interactions between the magnesia–chromite refractory and slags F1 and F2, respectively. As seen in Figs. 14(a) and 15(a), slags F1 and F2 are unsaturated with respect to both refractory phases, i.e. the periclase solid solution and the spinel phase. For slag F1, the periclase solid solution is dissolved entirely until the slag reaches MgO saturation at 7.1 wt%. The spinel phase becomes stable soon after the periclase (Fig. 14(a)). As seen in Fig. 14(b), the  $\text{Cr}_2\text{O}_3$  content in the slag phase increases up to a maximum of 3.5 wt%, which corresponds to the point where the spinel solution becomes stable, and then decreases continuously.

Globally, the slag composition does not change significantly with increasing the amount of refractory up to  $x=0.8$ . The FeO content in the periclase solid solution (Fig. 14(c)) remains stable at about 15 wt%. The  $\text{Cr}_2\text{O}_3$  content in the solid solution increases to a maximum of 8.1 wt%, corresponding to the point the spinel phase becomes stable, and then remains constant. The spinel solution also exhibits approximately the same composition with increasing the amount of refractory. The stability of the refractory phases in contact with slag F2 is similar to that in contact with slag F1 (Fig. 15(a)). The periclase solid solution becomes stable once the MgO content has reached saturation at 7.3 wt% MgO in the slag. The  $\text{Cr}_2\text{O}_3$  content in the slag reaches a maximum of 3.2 wt% when the spinel phase becomes stable, then decreases (Fig. 15(b)). The FeO content in the slag decreases continuously with increasing the amount of refractory as the latter dissolves in the periclase solid solution and in the spinel phase (Fig. 15(c) and (d)). The maximum FeO content in the periclase solution and in the spinel is respectively 31.4 and 3.8 wt%. When the spinel phase is stable, the  $\text{Cr}_2\text{O}_3$  content in the periclase solid solution is constant at about 8.1 wt%. As mentioned before, the  $\text{SiO}_2$  and MgO contents in the slag increase sharply with increasing the fraction of refractory due to the dissolution of the refractory silicate phase in a very small amount of slag. The predictions are in reasonably good agreement with the observations. The main disagreement concerns the  $\text{Cr}_2\text{O}_3$  and FeO contents in the periclase solid solution. The measured  $\text{Cr}_2\text{O}_3$  content ( $\sim 15$  wt%) is significantly higher than the predicted values ( $\sim 8$  wt%), whereas the measured FeO content is lower than predicted. Also the MgO content in the infiltrating slag does not increase as such as predicted.

### 3.2.3. Degradation mechanisms

The degradation mechanisms of magnesia–chromite refractories have been investigated previously.<sup>19–31</sup> Magnesia–chromite bricks have attractive refractory properties, such as high hot temperature strength and good slag resistance. The presence of the secondary chromite phase prevents slag infiltration by providing direct bonding between magnesia grains. However, magnesia–chromite refractory suffers from the inactivation of the secondary chromite phase at elevated temperatures,<sup>19,30,32</sup> where the chromite components dissolve into the surrounding periclase grains to form

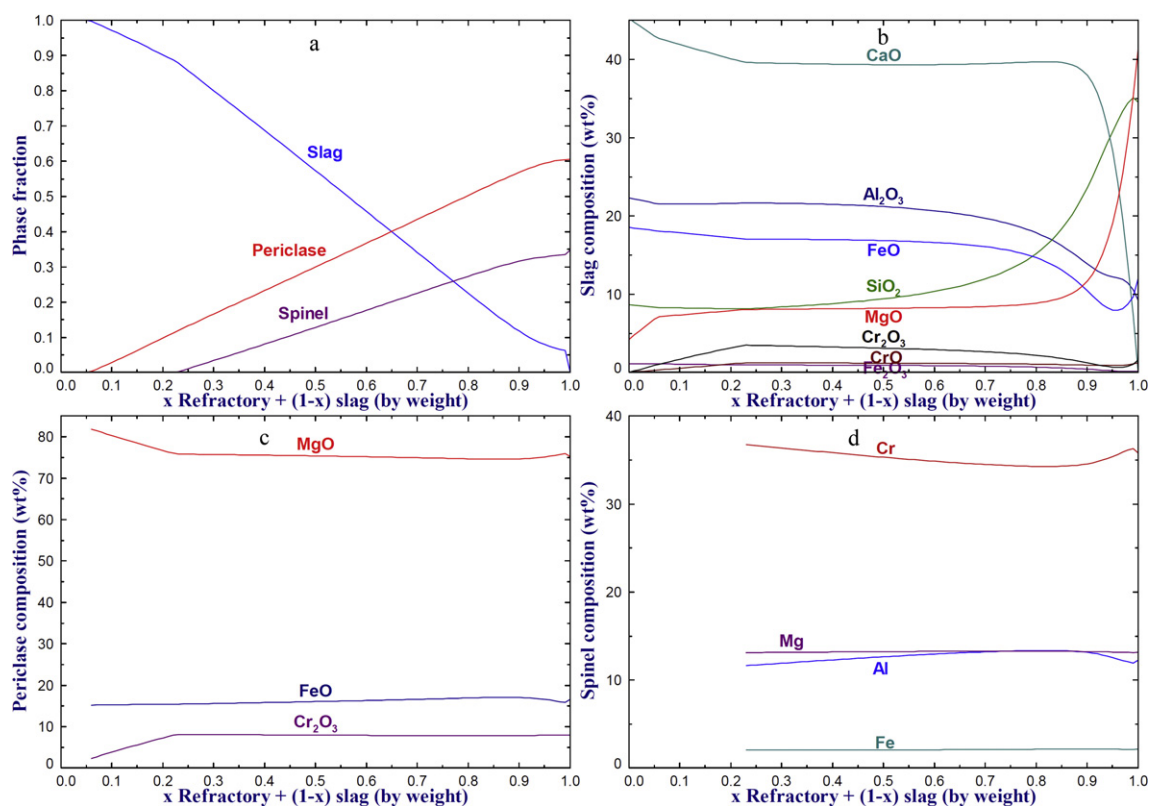


Fig. 14. (a) Predicted chemical stability and chemical composition of (b) slag, (c) periclase solid solution and (d) spinel after interaction between magnesia–chromite refractory and slag F1.

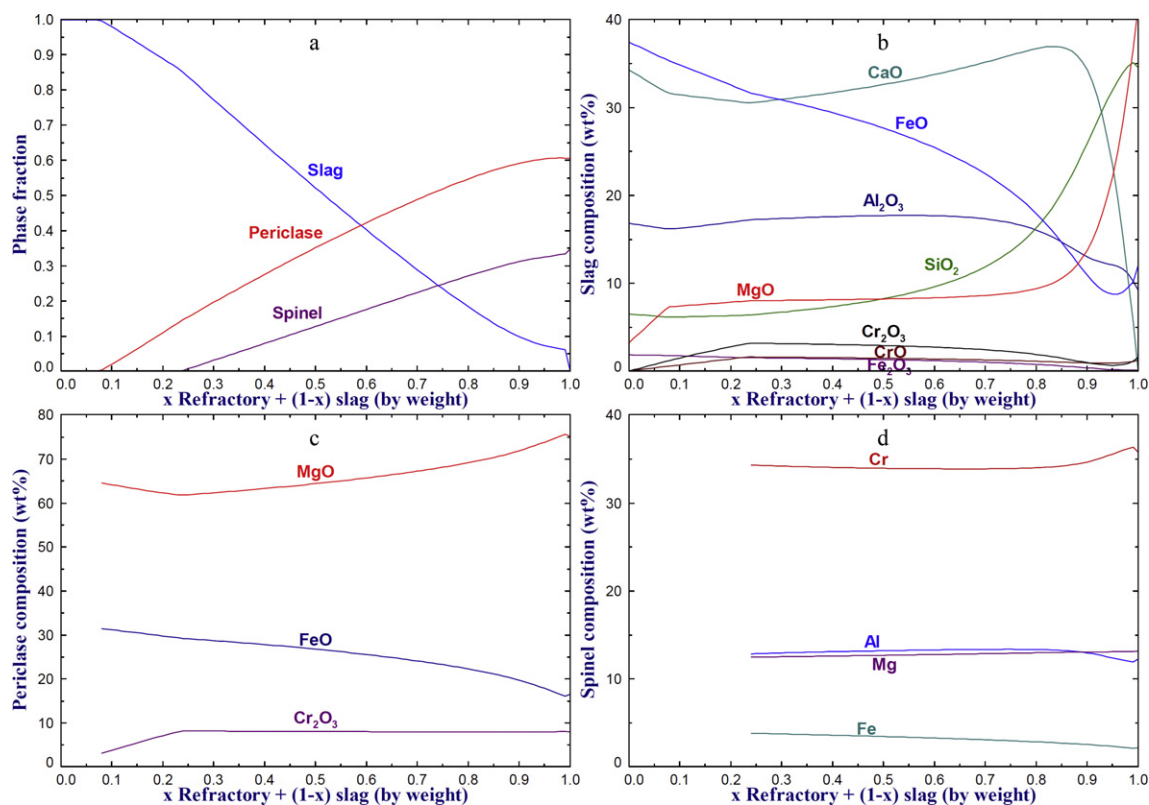


Fig. 15. (a) Predicted chemical stability and chemical composition of (b) slag, (c) periclase solid solution and (d) spinel after interaction between magnesia–chromite refractory and slag F2.

a (Mg,Cr,Fe,Al)O solid solution. As a result, the two-phase refractory transforms gradually into a one-phase refractory system, which is prone to slag infiltration along the grain boundaries. In general, it was found that the corrosion of magnesia–chromite refractories increases with decreasing the slag basicity.<sup>21,23</sup> Chromite was reported to be more resistant than periclase in acid slags, while periclase is more resistant than chromite at high basicity.<sup>21</sup> According to Guo et al.,<sup>31</sup> the dissolution of the primary chromite was increased with high  $\text{Al}_2\text{O}_3$  stainless steel slags. However, higher  $\text{Al}_2\text{O}_3$  content in slag promoted the formation of a spinel layer at the refractory/slag interface, which presumably protected the brick from major slag infiltration. Under low oxygen partial pressure and high temperature,  $\text{FeO}_x$  and  $\text{Cr}_2\text{O}_3$  decomposition to metallic Fe and Cr takes place from the primary and secondary chromite phases,<sup>30,31</sup> leading to a more severe refractory degradation.

Under the present experimental conditions, the corrosion mechanism of magnesia–chromite refractory consists of severe slag infiltration throughout the refractory, high temperature inactivation of the secondary chromite and dissolution of the primary chromite in the infiltrating slag. The level of remaining secondary chromite was significantly diminished and completely disappeared in some areas. Within 10 min of interaction, the refractory was completely infiltrated by slag through the open pore network and along the periclase grain boundaries. The secondary chromite phase was found to be gradually inactivated through dissolution in the surrounding periclase phase and in the infiltrating slag. Cr preferentially dissolved in the periclase solid solution, whereas Fe dissolved in the periclase solid solution and in the infiltrating slag. MgO was also found to dissolve in the infiltrating slag. The observed corrosion behavior is in good agreement with the predictions, except for Cr. Further corrosion is expected with longer immersion time as the theoretical MgO saturation is not reached, especially for slag C2. Though the  $\text{Al}_2\text{O}_3$  content in the slag is comparable to the study of Guo et al.,<sup>31</sup> no spinel layer formation was observed at the slag/refractory interface. The contact time is probably too short or saturation with regards to the spinel components was not reached locally.

With the loss of the secondary chromite, the normal brick bonding was gradually replaced by a liquid bonding, which rendered the refractory highly vulnerable to erosion under turbulent flow conditions. As the refractory is severely slag infiltrated, crack formation and spalling might occur due to high internal stresses between the infiltrated and non infiltrated zones arising from the densification of the brick.<sup>30</sup> With higher FeO contents in the slag, the refractory degradation seems more severe as the periclase grains appeared to be pushed apart by the infiltrating slag, leading to more severe erosion conditions. The FeO content in the periclase solid solution was found to be high as FeO from the slag dissolved at the periclase grains edges. A possible explanation for this behavior was given by Jones et al.<sup>19</sup> following the study of White and Richmond.<sup>33</sup> The dissolution of iron oxide into the periclase solid solution decreases the dihedral angle between periclase grains for the periclase-slag system, which renders the refractory system less resistant to slag ingress.

#### 4. Summary

Two typical RH refractories, magnesia–carbon and magnesia–chromite refractories, were immersed into five different slags for 10 min at 1600 °C in an induction furnace to investigate the refractory degradation mechanisms during the RH process: a typical ladle slag, two FeO-rich slags containing 20 and 40 wt% FeO, and two CaO– $\text{Al}_2\text{O}_3$  slags. Microstructural investigations of the as-delivered and worn refractories were carried out to study the interactions between slag and refractory. In addition, thermodynamic calculations were performed to assist with the interpretation of the experimental results.

Corrosion of magnesia–carbon refractory by the ladle slag and the CaO– $\text{Al}_2\text{O}_3$  slags C1 and C2 was limited as the refractory carbon phase efficiently prevented slag infiltration. According to the thermodynamic calculations, the main degradation mechanism for slags C1 and C2 is the dissolution of MgO from the refractory to the unsaturated slag. From the experimental observations, only a limited increase of the MgO content at the refractory hot face was found and the overall sample degradation was very limited. In contrast, severe magnesia–carbon refractory degradation was observed in contact with the two FeO-rich slags, in agreement with the thermodynamic predictions. The refractory carbon phase was oxidized by FeO with formation of Fe metal droplets at the refractory hot face. As a result, a large decarburized layer was formed at the slag refractory interface, which was infiltrated by the slags. The MgO grains in the decarburized layer could be then exposed to the slags, leading to their dissolution and erosion to the slags.

The magnesia–chromite refractory was entirely infiltrated by all five slags within 10 min interaction time. The corrosion mechanism consists of severe slag infiltration throughout the refractory, high temperature inactivation of the secondary chromite and dissolution of the primary chromite in the infiltrating slag. The secondary chromite phase was found to be gradually inactivated through dissolution in the surrounding periclase phase and in the infiltrating slag. With the loss of the secondary chromite, the normal brick bonding was gradually replaced by a liquid bonding, which rendered the refractory highly vulnerable to erosion under turbulent flow conditions. With higher FeO contents in the slag, the refractory degradation seems more severe as the periclase grains appeared to be pushed apart by the infiltrating slag, leading to more severe erosion conditions.

From the present study, it was found that magnesia–carbon refractory shows superior corrosion resistance to magnesia–chromite in contact with normal ladle slag and CaO– $\text{Al}_2\text{O}_3$  type slag. However, magnesia–chromite refractory can exhibit higher corrosion resistance against high FeO slag than magnesia–carbon refractory.

#### Acknowledgements

This project was supported by RIST, Korea. The partial financial support by a CRD grant from the Natural Sciences and



Engineering Research Council of Canada in collaboration with Posco, RIST and Tata Steel Europe is also appreciated.

## References

- [1]. Van Ende M-A, Kim Y-M, Cho M-K, Choi JH, Jung I-H. A kinetic model for the Ruhrstahl Heraeus (RH) degassing process. *Metall Mater Trans B* 2011;**42B**(3):477–89.
2. Bale CW, Bélisle E, Chartrand P, Decterov SA, Eriksson G, Hack K, Jung IH, Kang YB, Melançon J, Pelton AD, Robelin C, Petersen S. FactSage thermochemical software and databases—recent developments. *Calphad* 2009;**33**(2):295–311.
3. Pickering GD, Batchelor JD. Carbon–MgO reactions in BOF refractories. *Am Ceram Soc Bull* 1971;**50**(7):611–4.
4. Leonard RJ, Herron RH. Significance of oxidation–reduction reactions within BOF refractories. *J Am Ceram Soc* 1972;**55**(1):1–6.
5. Carniglia SC. Limitations on internal oxidation–reduction reactions in BOF refractories. *Am Ceram Soc Bull* 1973;**52**(2):160–5.
6. Yamaguchi A. Control of oxidation–reduction in magnesia–carbon refractories. *Taikabutsu Overseas* 1984;**4**(1):32–7.
7. Watanabe A, Takahashi H, Nakatani F. Mechanism of dense magnesia layer formation near the surface of magnesia–carbon brick. *J Am Ceram Soc* 1986;**69**(9):C213–4.
8. Pierard J, Sichen D, Jonsson P, Seetharaman S, Landin T. Effect of slag on carbon bearing MgO refractories. *Ironmak Steelmak* 1998;**25**(5):374–81.
9. Lee WE, Moore RE. Evolution of in situ refractories in the 20th century. *J Am Ceram Soc* 1998;**81**(6):1385–410.
10. Lee WE, Zhang S. Melt corrosion of oxide and oxide–carbon refractories. *Int Mater Rev* 1999;**44**(3):77–104.
11. Baudin C, Alvarez C, Moore RE. Influence of chemical reactions in magnesia–graphite refractories: I. Effects on texture and high-temperature mechanical properties. *J Am Ceram Soc* 1999;**82**(12):3529–38.
12. Baudin C, Alvarez C, Moore RE. Influence of chemical reactions in magnesia–graphite refractories: II. Effects of aluminum and graphite contents in generic products. *J Am Ceram Soc* 1999;**82**(12):3539–48.
13. Zhang S, Lee WE. Influence of additives on corrosion resistance and corroded microstructures of MgO–C refractories. *J Eur Ceram Soc* 2001;**21**(13):2393–405.
14. Smets S, Parada S, Weytjens J, Heylen G, Jones PT, Guo M, Blanpain B, Wollants P. Behaviour of magnesia–carbon refractories in vacuum–oxygen decarburisation ladle linings. *Ironmak Steelmak* 2003;**30**(4):293–300.
15. Van Ende MA, Guo MX, Jones PT, Blanpain B, Wollants P. Degradation of MgO–C refractories by MnO-rich stainless steel slags. *Ceram Int* 2009;**35**(6):2203–12.
16. Zhang S, Sarpoolaky H, Marriott NJ, Lee WE. Penetration and corrosion of magnesia grain by silicate slags. *Br Ceram Trans* 2000;**99**(6):248–55.
17. Shirasuka K, Yamaguchi G. Phenomenon of exsolution precipitates in the periclase solid solution of the system MgO–Al<sub>2</sub>O<sub>3</sub>–Fe<sub>2</sub>O<sub>3</sub>–Cr<sub>2</sub>O<sub>3</sub>. *Yogyo Kyokaishi* 1976;**84**(6):271–8.
18. Goto K, Lee WE. The direct bond in magnesia chromite and magnesia spinel refractories. *J Am Ceram Soc* 1995;**78**(7):1753–60.
19. Jones PT, Vleugels J, Volders I, Blanpain B, Van der Biest O, Wollants P. A study of slag-infiltrated magnesia–chromite refractories using hybrid microwave heating. *J Eur Ceram Soc* 2002;**22**(6):903–16.
20. Leonard RJ, Herron RH. Volume expansion and structural damage in periclase–chrome refractories. *Am Ceram Soc Bull* 1972;**51**(12):891–5.
21. Calkins DJ, Gilbert V, Saccomano JM. Refractory wear in the argon–oxygen–decarburization process. *Am Ceram Soc Bull* 1973;**52**(7):570–4.
22. Whitworth DA, Jackson FD, Patrick RF. Fused basic refractories in the argon–oxygen decarburization process. *Am Ceram Soc Bull* 1974;**53**(11):804–8.
23. Narita K, Onoye T, Satoh Y, Taniguchi K. Slag testing of refractories for ladle refining by ESR method. *Taikabutsu* 1984;**36**(316):273–7.
24. Kyoden H, Ichikawa K, Iwado H. Texture and slag resistance of commercial fused magnesia–chrome clinkers. *Taikabutsu* 1985;**37**(328):284–90.
25. Takahashi H, Kawakami T, Oguchi Y, Tsuchiya I, Uzaki N. Application of high chromia magnesia chrome refractories to secondary refining systems. *Taikabutsu* 1988;**40**(9):564–6.
26. Wiederhorn SM, Krause Jr RF, Sun J. Effect of coal slag on the microstructure and creep behavior of a magnesium chromite refractory. *Am Ceram Soc Bull* 1988;**67**(7):1201–10.
27. Engel R, Marr R, Pretorius E. Refractory/slag systems for ladles and secondary refining processes. Part XIII. *Iron Steelmak* 1997;**24**(4):59–60.
28. Mosser J, Buchebner G, Dosinger K. New high-quality MgO–Cr<sub>2</sub>O<sub>3</sub>-bricks and Cr-free alternatives for the lining of RH/DH-vessels. *Veitsch-Radex Rundschau* 1997;(1):11–23.
29. Jones PT, Blanpain B, Wollants P, Hallemans B, Heylen G, Weytjens J. Extending the life of ALZ NV's VOD ladle lining. *Iron Steelmak* 1999;**26**(12):31–5.
30. Jones PT, Blanpain B, Wollants P, Ding R, Hallemans B. Degradation mechanisms of magnesia–chromite refractories in vacuum–oxygen decarburisation ladles during production of stainless steel. *Ironmak Steelmak* 2000;**27**(3):228–37.
31. Guo M, Jones PT, Parada S, Boydens E, Van Dyck J, Blanpain B, Wollants P. Degradation mechanisms of magnesia–chromite refractories by high-alumina stainless steel slags under vacuum conditions. *J Eur Ceram Soc* 2006;**26**(16):3831–43.
32. Jones PT, Desmet D, Guo M, Durinck D, Verhaeghe F, Van Dyck J, Liu J, Blanpain B, Wollants P. Using confocal scanning laser microscopy for the in situ study of high-temperature behavior of complex ceramic materials. *J Eur Ceram Soc* 2007;**27**(12):3497–507.
33. White J, Richmond C. Recent developments in research on basic refractories. 2. Microstructural relations in basic refractories. *Refractories J* 1970;**46**:6–18.